Quantum and classical field scattered on a single two-level system

S. A. Gunin [1,2,*] A. Yu. Dmitriev,[1,3] A. V. Vasenin [1,2] K. S. Tikhonov [1,4] G. P. Fedorov [1,3,5] and O. V. Astafiev[2,1]

[1]*Moscow Institute of Physics and Technology, Dolgoprudniy 141700, Russia*
[2]*Skolkovo Institute of Technology, Moscow 121205, Russia*
[3]*Russian Quantum Center, Skolkovo Village 143025, Russia*
[4]*Landau Institute for Theoretical Physics, Moscow 119334, Russia*
[5]*National University of Science and Technology, MISIS, Moscow 119049, Russia*

In many problems, the scattering amplitudes of a weak coherent pulse are almost equivalent to the ones of a single propagating photon. We thoroughly compare the scattering of (i) a short microwave coherent pulse from a rf generator and (ii) a vacuum-photon coherent superposition from the two-level emitter, both directed to a single two-level system—the probe. To do that, we use two superconducting qubits to implement emitter and probe, both strongly coupled to the same waveguide. However, with the use of a magnetic circulator we couple the field from the emitter to the probe without reverse backaction, thereby working with a cascaded atomic system implemented in a waveguide-QED setup. By measuring the dynamics of the scattered field, we find a certain discrepancy between two cases, confirmed by analytical and numerical study. Particularly, we find the optimal amplitude Ω_* of classical pulse mimicking the superposition from the emitter, for which the difference becomes very small (but nonvanishing) and is almost unavailable to measure in practice.

I. INTRODUCTION

An artificial superconducting atom is a promising platform for studying fundamentals of light-matter interaction due to the ability to achieve strong coupling with an open space or single-mode fields [1,2]. Over the past two decades many quantum optical experiments demonstrating various properties of light were conducted: Resonance fluorescence of the single qubit [3], wave mixing [4], and single-photon routing [5]. Moreover, since the cavity quantum electrodynamics (cQED) platform provides a highly efficient on-demand single-photon source [6] it is possible to study scattering of various light states on atoms strongly coupled to an open one-dimensional (1D) space. Studying the interaction of light having arbitrary statistics with the single atom has a long-term theoretical interest [7–9]. However, previous works considering one-dimensional photon transport [10] focus mostly on the law of scattering of field in pure Fock or coherent states [11–16] and on the dynamics of population [17–19] after interaction. Moreover, the properties of the fields scattered in the superposed Fock state have not received sufficient coverage.

In the present work, we study both theoretically and experimentally scattering of the single-photon pulses being in the zero-one superposed Fock state—hereinafter it is called "quantum" pulse—on the superconducting transmon qubit, and subsequently compare obtained results with the case of scattering of an exponentially modulated coherent pulse; henceforward it is called "classical." The quantum pulse generated by the single-photon source lacks states $|n\rangle$ with $n > 1$.

Therefore, the scattering of such a pulse would not result in more than one atomic Rabi oscillation, which, in general, is not the case for the coherent pulse, which, if strong enough, may force to exhibit multiple atomic population oscillations. Population oscillations are connected with the scattered field envelope oscillations. Measuring the time-domain envelope of the scattered field, we find that, in the limit of small field amplitude of the coherent signal, the experiment shows practically indistinguishable dynamics of the scattered fields, compared to the scattering of antibunched light, due to the relatively small impact of the higher-order Fock states present in the coherent pulse [20,21].

However, we theoretically show that the scattered field dynamics has non-negligible differences in the two cases for arbitrary choice of coherent pulse parameters. Furthermore, we estimate the coherent field amplitude yielding the closest classical approximation of the scattered field dynamics compared to the quantum case. Hence, in the low-signal limit, one is able to consider single-photon approximation in a wide range of problems, as in the single-photon microwave range detector [22].

II. EXPERIMENTAL RESULTS

A. Device and measurement setup

To explore the stated scattering problem, we implement a cascaded [9,23] system from two superconducting artificial atoms—tunable transmon qubits [24]; see Fig. 1. The first atom is coupled to a pair of semi-infinite waveguides, implementing a single-photon source (which we will call emitter) [6]. The emitter qubit is designed similarly to the emitter
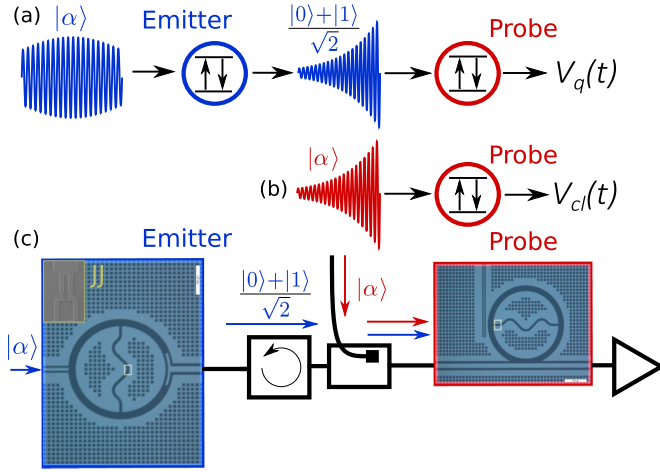
---

*gunin.sa@phystech.edu

FIG. 1. (a) Schematic problem statement for the scattering of the quantum signal being produced from the emitter qubit on the probe qubit. (b) Schematic problem statement for the scattering of the coherent signal on the probe qubit. (c) Schematic describing the connection between sample holders. Blue lines denote the signal path in scattering of the single-photon pulses; red lines denote the signal path in scattering of the coherent pulses. An output amplification line is common for both experiments. Optical images of the emitter qubit and the probe qubit are presented. The yellow box on (c) contains a scanning electron micrograph of the Josephson junctions.

in [25]. It may be excited by a driving pulse applied via the weakly coupled control line, which prepares an arbitrary single-photon superposed state; subsequently it radiates into the strongly coupled emission line. The field emitted to the output waveguide propagates through a circulator and then interacts with the probe (quantum scatterer) qubit, which is side coupled to the waveguide. We subsequently detect the voltage in this waveguide $V_q(t)$; see Fig. 1(a). The circulator prevents the backaction of the probe qubit on the emitter qubit [7,26]. We estimate power loss between the output of the emitter and the coupling point of the probe atom to be about 3 dB.

The emitter and probe are located on two different silicon chips and placed into two separate sample holders with separate permalloy magnetic shield. Each sample holder has its own magnetic coil, which allows one to change magnetic fluxes and thereby to tune the working frequencies of the devices. The output signal from the probe is then amplified by cryogenic and room-temperature amplifiers. After amplification, the signal is down-converted by a standard heterodyne scheme with double balanced [27] quadrature mixers in the single-sideband modulation regime. Typical incoming to the mixer waveforms generated from fast AWG have 1 GSa/s sampling rate and LO resolution is of the order of ∼1 Hz. Both quadratures are digitized with fast ADCs at the 1.25 GSa/s rate with the typical number of experimental trace averages of 2^{24} (approximately 10^7). Moreover, due to the possibility of independent tuning of the qubit frequencies, it is possible to detect the incoming pulse and output field separately. The incoming pulse is independently recorded and subtracted from the experimental traces to obtain what we call the "scattered" field.
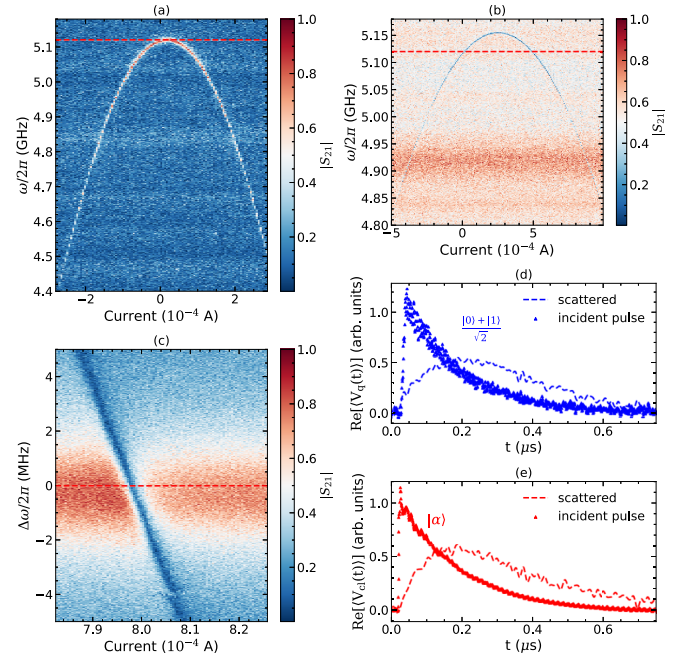

FIG. 2. (a) Single-tone spectroscopy of the bare emitter; the red dashed line represents the sweet-spot location ω_c. The emission line of the probe is represented at (b); the red dashed line is located at $\omega = \omega_c$. When qubits are tuned into resonance the transmission dip occurs at $\omega = \omega_c$ (c), the probe is tuned throughout the emitter's resonance, the emitter is located at sweet-spot frequency ω_c, and detuning $\Delta\omega$ between scanning frequency ω and emitter sweet-spot ω_c is defined as $\Delta\omega = \omega - \omega_c$. (d) The envelope of single-photon superposition spontaneously radiated after the $\pi/2$ pulse from the emitter (incident on the probe; the probe is far detuned) at a frequency of ω_c is digitized and plotted as blue triangles. Scattering on the probe field after interaction with the incident quantum pulse is plotted as a blue dashed curve. (e) The coherent pulse with the exponential envelope excites the probe at ω_c frequency. Incident exponential pulse is plotted as a red dashed line. The envelope of the scattered field on the probe is represented with red triangles.

The classical coherent signal may be applied directly to the probe qubit via a directional coupler without disturbing the emitter and we denote the field scattered in this experiment as $V_{cl}(t)$; see Fig. 1(b). Therefore, the presented setup allows one to study the scattering of an equal single-photon superposition $(|0\rangle + |1\rangle)/\sqrt{2}$ state) pulse or classical pulses on the probe qubit, since the output line is common; see Fig. 1(c). The full experimental setup is presented in Appendix C.

B. Device characterization

First, we characterize the energy level structure of the discussed devices. Hence we provide elastic scattering data of continuous waves for emitter and probe qubits. Figure 2(a) presents the spectrum of the emitter with the probe being far detuned versus bias current in a coil, generating a magnetic field, which penetrates a SQUID. The sweet-spot position of the emitter is located at $\omega_c/2\pi = 5.119$ GHz; see the dashed red line in Fig. 2(a). Hereinafter, ω_c would be a carrier frequency for the subsequent experiments.

Similarly, we record the bare spectrum, see Fig. 2(b), of the probe qubit, using a different excitation line as illustrated via red arrows in Fig. 1(c). The probe's sweet spot slightly differs from the emitter's one, $\omega_p/2\pi = 5.153$ GHz. Therefore, in order to study resonant scattering we should fix the frequency ω_c and precisely tune the probe into resonance with ω_c. As soon as the output of the emitter at the frequency ω_c passes through the waveguide with the probe being tuned to the ω_c, one can observe the transmission dip caused by the probe on the emission profile of the emitter and the emitter peak when they are detuned; see Fig. 2(c).

Next we proceed to time-resolved measurements, in order to characterize the relaxation rates of the qubits. We tune consecutively the emitter and the probe into resonance with the carrier frequency. The radiative linewidth of the probe equals $\Gamma/2\pi = 1.86$ MHz and for the emitter it is $\gamma/2\pi \simeq 1.85$ MHz.

Knowing the relaxation rates, we are able to study resonantly scattered fields either after interaction of the probe with the antibunched light, generated by the emitter qubit, or with the coherent pulse of the same width independently scattered on the probe. We generate equal vacuum-photon superposition $(|0\rangle + |1\rangle)/\sqrt{2}$ by sending an 8-ns-long $\pi/2$ pulse in the control line of the emitter, which is calibrated by measurement of Rabi oscillations on the emitter qubit via sweeping the duration of the excitation pulse in the control line. So, the averaged emitted field is the exponentially decaying wave packet; see blue triangles in Fig. 2(d). If we tune the probe into the resonance with the emitter (and also with the driving pulse), what we observe is the exponential pulse interference with the field scattered by a probe qubit; scattered field quadrature is presented in Fig. 2(d) as a blue dashed line.

In the case of coherent (classical) pulse scattering, we apply exponentially modulated pulses and measure the average transmitted field with the probe being either in resonance with the carrier or out of it. The original pulse transmitted through the waveguide is recorded when the probe is far detuned; see red triangles in Fig. 2(e). If the probe is in resonance with the carrier, see the red dashed line Fig. 2(e), we obtain the scattered pulse by subtracting the independently measured incoming pulse (red triangles) from the experimental data. The similarities and differences between resonantly scattered fields in the two described experiments are analyzed below.

C. Single-photon pulse scattering

First, we experimentally study details of the single-photon (quantum) scattering case. We record the field envelopes $V_q(t)$, see Fig. 1(a), with respect to detuning $\Delta = \omega_c - \omega$ between single-photon carrier frequency ω_c, which always remains constant, and probe frequency ω_p. The probe coil current is tuned nonlinearly, using recorded earlier spectra, in order to achieve linear slope in the probe frequency. Detected field envelopes $V_q(t)$ with respect to detuning contain the incoming single-photon pulse and the scattered part; they are presented in the left column of Fig. 3. The number of photons in the quantum pulse is not greater than one and, consequently, if the probe is in exact resonance with the quantum pulse, the envelope of the scattered signal does not behave in an oscillatory manner, which is a certain signature of the photon
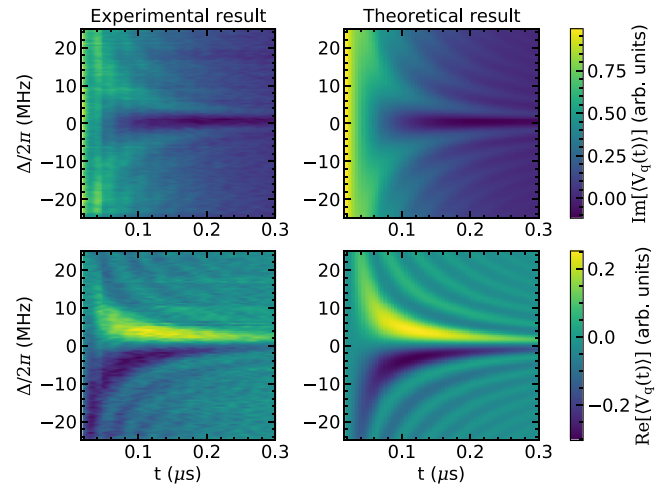

FIG. 3. Comparison of the detected (incoming + scattered) field envelope $V_q(t)$ in real time t with respect to detuning Δ between the photon carrier frequency ω_c and probe qubit frequency ω_p with the analytical results, see Eq. (3), in the case of a scattering single-photon pulse emitted from the emitter on the probe qubit. The color bars for the experimental and theoretical quadratures are the same. A complex scaling factor is used to fit the data.

statistics, since the contrary (Rabi oscillations in resonance) would require more than one photon. Instead, one observes a single extremum at around 200 ns after which the curve decays to zero. Beatings of the envelope for nonzero detunings are not connected with the multiphoton processes, but with the Ramsey fringes. Also we see that the scattered field patterns are symmetric (imaginary part) and antisymmetric (real part) with respect to the detuning sign. So the antisymmetric quadrature is exactly zero at zero detuning, and thus only the symmetric one should be further analyzed.

Next, we analyze the problem analytically. The field $V_e(t)$ with the amplitude A_e emitted by the emitter into the waveguide with impedance Z_e at the frequency ω_c is proportional to the expectation value of lowering operator for the emitter $\langle \sigma_-^e \rangle$:

$$V_e(t) = A_e \sqrt{\gamma} \langle \sigma_-^e(t) \rangle, \tag{1}$$

where the constant $A_e = i\sqrt{\hbar\omega_c Z_e}$ is the same for any field scattered by the probe, and further it will be omitted. For typical parameters, the field amplitude is approximately 10^{-8} V before amplification. This field amplitude has no adjustable parameters and the envelope shape is completely defined by the state of the emitter. For the equal single-photon superposition we have $\langle \sigma_-^e \rangle(t) = \frac{\exp(-\gamma_2 t)}{2}$, where $\gamma_2 = \frac{\gamma}{2} + \gamma_\phi$ is the dephasing rate of the emitter, γ is the radiative linewidth, and γ_ϕ is the pure dephasing.

An approach to obtain an analytical expression for the scattered field is to consider the isolated system of two atoms interacting via a continuum of waveguide modes further utilizing Weisskopf [28] approximation. Another approach is to include the interaction as a dissipationlike exchange term in the formalism of master equations [7,26]. Omitting the propagation delay time, the detected field consists of expectation values of lowering operators representing fields emitted by the

emitter and the field scattered by the probe:

$$V_q(t) = A_e\sqrt{\gamma}\langle\sigma_-^e(t)\rangle + A_p\sqrt{\Gamma}\langle\sigma_-^p(t)\rangle. \quad (2)$$

Here $A_p = \frac{A_e}{\sqrt{2}}$. After some calculations (see Appendix A), one obtains a formula for the total (the sum of incident and scattered) detected field:

$$V_q(t) \propto \sqrt{\gamma}\frac{e^{-\gamma_2 t}}{2} + \sqrt{\frac{\Gamma}{2}}\frac{\sqrt{\Gamma\gamma}(e^{-\gamma_2 t} - e^{-\Gamma_2 t + i\Delta t})}{\gamma - \Gamma + 2i\Delta}, \quad (3)$$

where $\Gamma_2 = \frac{\Gamma}{2} + \Gamma_\phi$ stands for the dephasing rate of the probe and Γ_ϕ is the pure dephasing. The first part of Eq. (3) is the incident field, while the second is the scattered part. The behavior of the analytically derived $V_q(t)$, see right column of Fig. 3, agrees fairly well with the measurement data. We clearly see that, in the resonant case, the envelope does not oscillate, which is again a manifestation of not more than a single photon within the incoming pulse. However, for nonzero detunings the envelope oscillates with the detuning frequency Δ, which is in agreement with our measurements. The model used for fit accounts for the arbitrary complex scaling prefactor. The phase of the prefactor is determined using the resonance condition: One quadrature of the scattered field should be trivial in the case of the resonant scattering.

Agreement of the experimentally obtained patterns and theoretical models [Eq. (3)] allows one to extrapolate from the experimental data to the wider range of the scattering parameters, namely, radiative linewidths and detunings. We utilize this fact for future discussions. Moreover, since we used a typical open-system approach assuming Markovian bath, the result obtained is quite general and could potentially be extrapolated to other types of TLS disregarding their nature.

D. Coherent pulse scattering

For the quantum pulse, the scattered field part is fully defined [see Eq. (3)] via radiative linewidths of the probe and emitter. Therefore, it is possible to experimentally compare quantum case scattering with the classical analog using only the classical incident pulse of exponential shape with a known decay rate. We choose the case of resonant scattering as it is the most convenient, since we avoid field oscillations, which are not connected with the differences in photon statistics of the pulse. Hence we fix the frequency and obtain the scattered field $V_{cl}(t)$, with respect to amplitude Ω_0 of the coherent exponentially modulated pulse.

The pulse is applied to the probe atom and its amplitude can be described by the effective Rabi frequency $\Omega(t) = \Omega_0 e^{-\gamma_2 t}$ [29]. The amplitude Ω_0 of the classical pulse is a free parameter setting up the mean number of photons in the pulse. Experimentally measured field traces and theoretical as well with respect to Ω_0 are presented in the upper panel of Fig. 4. The incoming exponential pulse is digitally removed. Since measurements are performed in the resonance condition, the only quadrature is plotted, since the other quadrature is trivial. We are interested in the case of single envelope oscillation, which is the closest classical analog of single-photon scattering. The scattered field depends on the ratio between Ω_0 and Γ. If $\Omega_0 \gg \Gamma$, then the probe undergoes Rabi oscillations (for
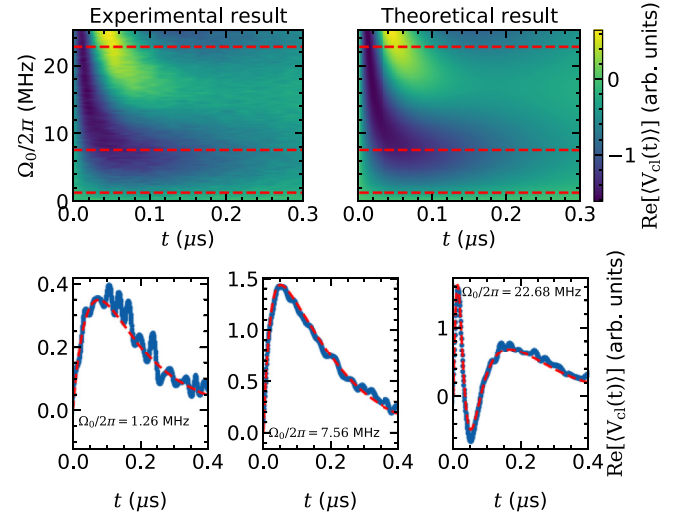

FIG. 4. Comparison of scattered (incoming subtracted) field envelopes $V_{cl}(t)$ (in resonance condition between the carrier frequency of the incoming exponentially modulated pulse and the probe) in the time domain t with respect to the strength Ω_0 of the driving pulse with theoretical results in the case of classical field scattering. The color bars of the experimental and theoretical quadratures are the same. Red dashed lines on the color maps are the cuts for different Ω_0. Corresponding traces are plotted in the bottom panels: Dashed red line is the theoretical fit; blue dots are the experimental traces.

instance, see the bottom right panel of Fig. 4). We measure the scattered field for different values of Ω_0; for future analysis we limit ourselves to the case of the $\Omega_0/2\pi \ll 10$ MHz, which is the limit of $\Gamma \sim \Omega_0$. In the regime of $\Omega_0 \sim \Gamma$ the average number of photons in classical pulse may be less than one and the scattering is more similar to the quantum case.

As in the previous section, we proceed to describe the scattered coherent pulse with an analytical model. To describe the scattering of the coherent pulse with the exponential envelope, we look for the solution of the master equation in Lindblad form for the Hamiltonian $H = \Omega_0/2 e^{-\gamma_2 t}\sigma_x$. In the resonance case, the equations are

$$\partial_t\langle\sigma_y\rangle = -\Omega_0\langle\sigma_z\rangle e^{-\gamma_2 t} - \frac{\Gamma}{2}\langle\sigma_y\rangle,$$

$$\partial_t\langle\sigma_z\rangle = -\Gamma(1 + \langle\sigma_z\rangle) + \Omega_0 e^{-\gamma_2 t}\langle\sigma_y\rangle. \quad (4)$$

The solution could be found as a series expansion in powers of Ω_0; see Appendix B for a detailed procedure. In the first order, we get the linear in Ω_0 part of the answer:

$$V_{cl}^{(1)}(t) = \sqrt{\frac{\Gamma}{2}}\frac{\Omega_0(e^{-\gamma_2 t} - e^{-\Gamma_2 t})}{\gamma - \Gamma}. \quad (5)$$

Even orders have zero contribution, but odd corrections are nonzero and decrease polynomially with respect to Ω_0. The analytical solution is presented in the bottom panel of Fig. 4. One can find a good correspondence of the experimental result with the analytical expressions. The scattered field envelope continuously transforms to the case of two atomic oscillations as the amplitude of the exciting signal increases. Additional oscillations on top of the general envelope are caused by digital filtering of the down-converted signal. The only fit
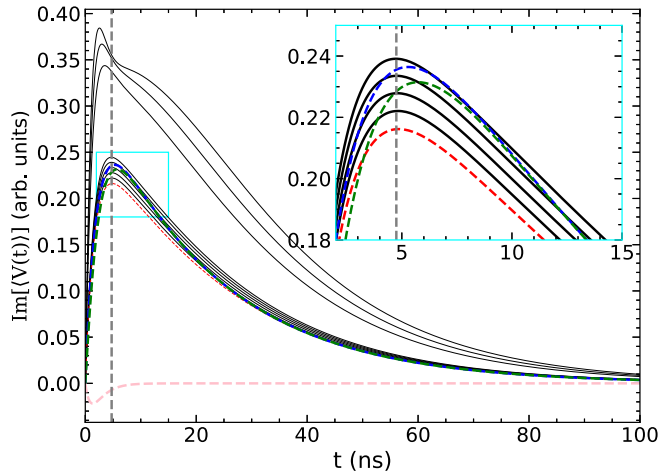
FIG. 5. Calculated scattered fields in both quantum and classical cases (the incoming exponential pulse is omitted in all cases). Red dashed line: the numerical solution (matches the full analytical solution) of the master equation with classical input pulse with $\Omega_0/2\pi = \sqrt{\gamma\Gamma}/2\pi = 0.3$ MHz. Black solid lines: the same for $\Omega_0/2\pi$ (0.31, 0.32, 0.33, 0.34, 0.35, 0.6, 0.7, and 0.8) MHz. Blue dashed line: the solution of the master equation with quantum input pulse, which fully matches the (omitted for clarity) linear in Ω_0 part of the solution for the incoming exponential classical pulse with $\Omega_0 = \sqrt{\gamma\Gamma}$. Green dashed line: sum of two first nonzero contributions to the classical case solution with $\Omega_0/2\pi = 0.3$ MHz. Pink dashed line: the second nonzero (third order in Ω_0) contribution of the classical solution, $\Omega_0/2\pi = 0.3$ MHz.

parameter is the complex prefactor, so the color bars are the same.

Moreover, it is worth mentioning that leading order $V_{cl}^{(1)}$ fully matches the case when the only photon is reemitted by the probe qubit; however, that point is not the subject of the current discussion, since it requires generally more complex analytical treatment.

III. COMPARISON OF CLASSICAL AND QUANTUM SCATTERING

Now we are ready to thoroughly compare both scattering cases and extrapolate theoretically some results to the wider range of radiative linewidths, since experimentally we are limited in the accessible range of parameters. Since the only oscillation is present in the quantum case, one can potentially distinguish a nonclassical state in the field which constitutes an input for the probe, if the scattered field is measured. However, we note that for a very weak Rabi amplitude, the behavior of the emitted field is also nonoscillating. Thus we ask another, more complex question: Whether one is able to distinguish between the classical and quantum cases when the number of photons in the classical pulse approaches one, that is, the single oscillation case.

Analyzing the results of calculations, we observe the difference between classical and quantum cases. In Fig. 5, we present the full analytical solution for classical and quantum pulses together with successive approximations of the first and third order. As stated before, the single-photon superposition radiated from the emitter has the fixed amplitude defined by
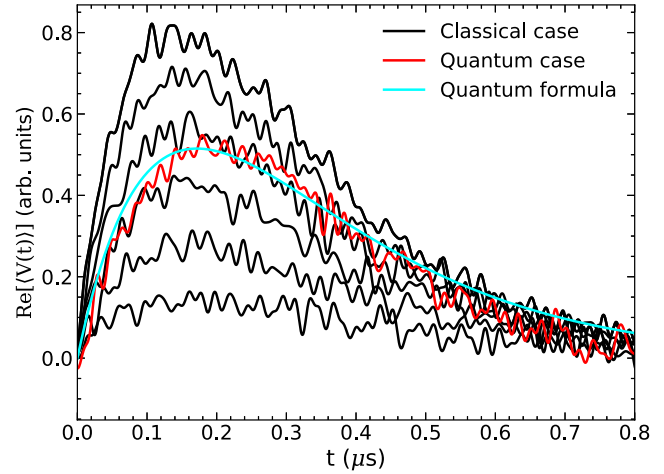

FIG. 6. Comparison of the experimentally obtained scattered fields in the resonance case in both quantum and classical cases omitting the incoming pulse. Scattering of the classical coherent pulse is provided with respect to the amplitude of the incoming pulse; corresponding $\Omega_0/2\pi$ frequencies are (0.27, 0.54, 0.81, 1.08, and 1.36) MHz. The quantum case is fitted with Eq. (3) (cyan solid line).

Eq. (3). Consequently, there is an optimal Rabi frequency Ω_* of classical pulse, for which the effect of this pulse on the probe is the most similar to the effect of the quantum superposition pulse. In other words, we could say that Ω_* is the effective "classical" amplitude of the quantum pulse. Comparing Eq. (3) and Eq. (5) we find that $\Omega_0 = \Omega_* \equiv \sqrt{\gamma\Gamma}$. Therefore, the quantum case solution Eq. (3) fully matches the first-order approximation of the classical case for $\Omega_0 = \Omega_*$. Importantly, Ω_* underestimates the value of the amplitude closely matching the quantum case.

In the limit of small $\Omega_0 \ll \Gamma$, one should expect a vanishing, but finite, difference between classical and quantum cases for any ratio between γ and Γ. For $\Omega_0 \gtrsim \Gamma, \gamma$ the waveform changes and starts to behave in an oscillatory manner, which is a readily detectable difference of behavior (the calculation is made for $\gamma/2\pi = 0.09$ MHz and $\Gamma/2\pi = 1$ MHz, giving the most prominent picture). Maxima positions in two cases are shifted, see Fig. 5, but the shift is relatively small and it is an open question whether it could be measured with existing technical limitations of a waveguide-QED setup since impedance mismatches and low signal-to-noise ratio could potentially overshadow the effect.

We also demonstrate comparison of the experimentally measured field envelopes for both classical and quantum cases in Fig. 6. It is impossible here to clearly distinguish the difference in envelopes. However, the closest classical signal could be determined in terms of Rabi amplitudes. $\Omega_*/2\pi = 1.02$ MHz results in the best approximation of the quantum answer to the classical one, which is slightly lower than $\sqrt{\Gamma\gamma}/2\pi \simeq 1.855$ MHz. The answer why the theoretically expected value is almost always smaller lies in the behavior of the other expansion terms. As it is shown in Fig. 5, consequent expansion terms pull down the signal level. Also, we have several sources of errors in the real experiment. First of all, the initial state of the probe qubit is not a pure ground state, though the temperature is still low. The second source is the
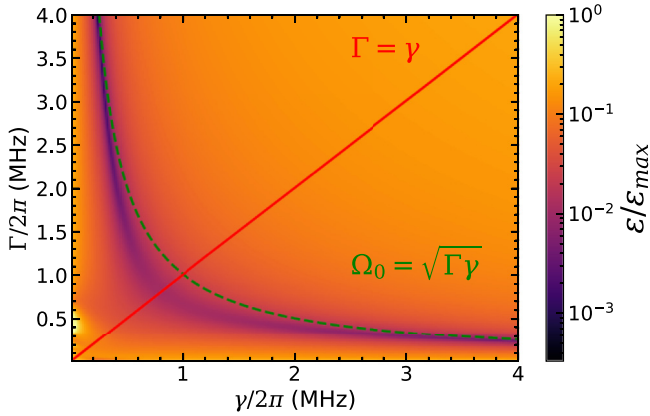
FIG. 7. Normalized dependence of the integral distance ϵ between calculated scattered fields in the quantum and classical case on the relaxation decay rates of emitter and probe qubits. The amplitude of the classical signal is chosen to be $\Omega_0/2\pi = 1$ MHz. The green line represents the harmonic mean of the relaxation rates of atoms; the red line is the mean line in the Γ, γ coordinates.

emission during the drive of the emitter (when preparing the superposed state), which also alters the initial state of the probe. It is hard to experimentally reduce such an effect, but it is small enough. The $\pi/2$ pulse is very short, but the pulse emitted is quite long, so we do not look at the short part (8 ns at the beginning can be neglected). Moreover, in some sense, we try to approximate the α coefficient in the corresponding coherent state, giving the closest behavior of the mean-field quadrature. But if the first two coefficients of the coherent-state expansion are close to coefficients of the superposed single-photon state, then there are always the higher states involved, so we need to reduce amplitude below the theoretical prediction, which was derived considering only 0 and 1 Fock states. So, finding the best leading-order correspondence we always overestimate higher-order terms of the coherent-state expansion, namely, Fock states with $n > 1$. Still, further we imply that there is a regime where theoretical value converges to the optimal one.

Next, in order to compare results of different calculations we use the following integral distance norm between two functions:

$$\epsilon = \sqrt{\int_0^\infty dt \, \frac{(V_{cl} - V_q)^2}{(V_{cl} + V_q)^2}}, \qquad (6)$$

which is a positive-valued function of decay constants and classical amplitudes. Since ϵ is nothing more than the distance between two curves in the Euclidian space, it is a good measure to compare theories, since it is positively defined and becomes trivial only when two curves coincide. Therefore, if we see trivial value, we state that scattering processes are the same. The normalized value of ϵ/ϵ_{max}, where $\epsilon_{max} = \max_{\Gamma,\gamma} \epsilon$, is plotted in Fig. 7 for a fixed value of Ω_0 as a function of Γ and γ. The dark area in Fig. 7 is the region where the quantum case has the closest correspondence with the classical case. We see that for $\gamma = \Gamma$ the discrepancy is maximal and the optimal Ω_0 is slightly less than $\sqrt{\gamma\Gamma}$. Also we see pure maximum, which is the manifestation of Rabi-like oscillations in the classical case in the limit of $\Omega \gg \gamma$
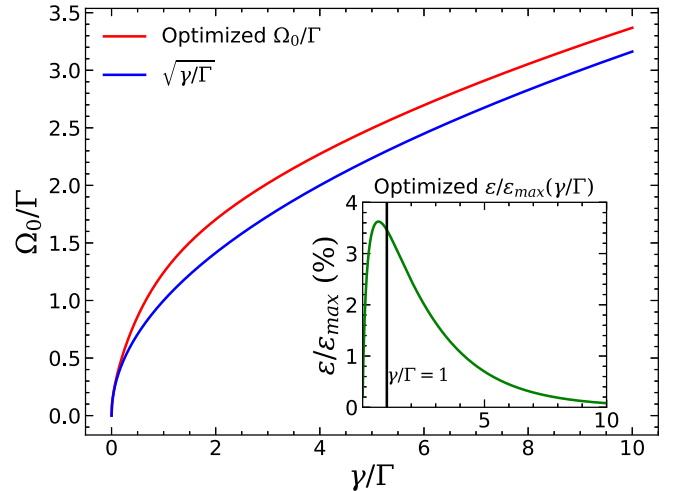

FIG. 8. Numerically optimized value of Ω_0 giving a minimum of the integral distance ϵ between the calculated scattered fields in both quantum and classical cases with respect to the ratio of decay times. The optimized value is compared with the harmonic mean of radiation rates divided by the relaxation rate of the probe qubit. An inset picture describes the dependence of ϵ on the ratio of decay times. Each point corresponds to a minimum of the difference between classical and quantum answers. All values except ϵ are calculated in units of Γ.

or, symmetrically, Γ. Still, one can note that the difference between the two answers still does not equal zero and never equals zero assuming any nonzero choice of radiative rates, since higher-order photon scattering processes are still present in the coherent signal. Therefore, we proceed with optimizing the ϵ numerically optimizing different values of Ω_0. In Fig. 8 we show minimal value of normalized ϵ obtained as a function of $\frac{\Omega}{\Gamma}$ for different $\frac{\gamma}{\Gamma}$ ratios. One can see that the optimal distance between classical and quantum curves has a distinct maximum. That result closely relates to the case of equal decay rates (inset figure), where we see that optimized Ω is close to the half of mean harmonic. Another noticeable feature is that in the limit of $\gamma \gg \Gamma$ the difference approaches zero, since the probe is almost not excited by the incoming pulse. The spectral width of the pulse would be so great compared to the linewidth of the probe qubit that the incoming pulse does not really identify the scattering potential. Another case is $\gamma \ll \Gamma$, where the qubit rapidly reemits incoming photons so that they almost do not excite it. Therefore, even though there are many photons in the field, the second system relaxes too quickly and the behavior is not very different from the single-photon case.

IV. CONCLUSION

We compared experimentally and theoretically the scattering of the quantum single-photon superposition pulse and classical exponentially decaying pulse on the probe superconducting artificial atom. Experimentally, we show that there is an optimal amplitude for the classical pulse, with which the behavior of the envelope of the scattered field is most similar to the quantum case. Also, we experimentally show the presence of the single field envelope oscillation in the

quantum case scattering. We show that there is a nonvanishing difference between the envelopes of the scattered fields in the wide range of decay rates, which could be potentially observed in the experiments with the greater SNR. The results of the work could be potentially extrapolated to the scattering of pulses with other nonclassical photon statistics or scattering on other systems, e.g., an equidistant three-level system.

ACKNOWLEDGMENTS

APPENDIX A: SOLUTION FOR THE QUANTUM CASE

The cascaded setup being considered could be typically assumed as a closed type system (two TLS and bosonic bath), while neglecting external drive nondiagonal drive terms. Therefore, one could expand pure vectors of state in a single-photon basis, due to the presence of an integral of motion, namely, $\Sigma_k \langle a_k^+ a_k \rangle + \Sigma_{i=1,2} \langle \sigma_+^i \sigma_-^i \rangle$. Thus the problem of quantum scattering could be reviewed in terms of pure states' formalism, expanded into a single-photon basis, allowing one to solve the system of ordinary differential equations, which can be modeled by means of Runge-Kutta methods or exactly solved proposing Markovian type approximations. On the other hand, we cannot omit drive terms in the case of classical signal scattering, due to continuous filling of Fock states in a coherent signal; thus the problem is more complex due to direct time dependence of coefficients in the equations. The system is described by the following Hamiltonian:

$$H = H_{\text{TLS}} + H_B + H_{I1} + H_{I2}, \tag{A1}$$

where two-level systems have different energy splittings,

$$H_{\text{TLS}} = \omega_e \hat{\sigma}_{1+} \hat{\sigma}_1 + \omega \hat{\sigma}_{2+} \hat{\sigma}_2, \tag{A2}$$

and the bosonic bath consists of left- and right-moving modes,

$$H_B = \int_0^{+\infty} (dk)\omega(k)\hat{a}_R^\dagger(k)\hat{a}_R(k) + \int_{-\infty}^0 (dk)\omega(k)\hat{a}_L^\dagger(k)\hat{a}_L(k), \tag{A3}$$

$$H_{I1} = \int_0^{+\infty} (dk)g_1[\hat{a}_L^\dagger(k)\hat{\sigma}_{1-} + \hat{a}_L(k)\hat{\sigma}_{1+}]. \tag{A4}$$

The first system interacts only with right-moving modes and the second system interacts with both left- and right-moving modes:

$$H_{I2} = \int_0^{+\infty} (dk)g_2[e^{-ikr}\hat{a}_R^\dagger(k)\hat{\sigma}_{2-} + e^{ikr}\hat{a}_R(k)\hat{\sigma}_{2+}^\dagger]$$
$$+ \int_{-\infty}^0 (dk)g_2[e^{-ikr}\hat{a}_L^\dagger(k)\hat{\sigma}_{2-} + e^{ikr}\hat{a}_L(k)\hat{\sigma}_{2+}^\dagger]. \tag{A5}$$

The system is prepared at $t = 0$ in the state

$$|\Psi\rangle = \frac{1}{\sqrt{2}}(|\uparrow\rangle + e^{i\phi}|\downarrow\rangle)|\downarrow\rangle|0\rangle. \tag{A6}$$

Note that this setup makes sense only for $r < 0$ (the first system, which is excited, interacts only with modes propagating to the left).

The number of photons never exceeds 1 and, at later times, the wave function can be written as follows:

$$|\Psi\rangle = \zeta(t)|\downarrow\rangle|\downarrow\rangle|0\rangle + \alpha_1(t)e^{-i\omega_e t}|\uparrow\rangle|\downarrow\rangle|0\rangle$$
$$+ \alpha_2(t)e^{-i\omega t}|\downarrow\rangle|\uparrow\rangle|0\rangle + \sum_k \beta_k(t)e^{-i\omega_k t}|\downarrow\rangle|\downarrow\rangle|k\rangle, \tag{A7}$$

$$\dot{\zeta}(t) = 0, \qquad \dot{\alpha}_1 = -ig_1 \int_{k<0} (dk)e^{-i(\omega_k - \omega_e)t}\beta_k,$$

$$\dot{\alpha}_2 = -ig_2 \int (dk)e^{-i(\omega_k - \omega)t}e^{ikr}\beta_k \tag{A8}$$

and the equation for the field's amplitudes:

$$\dot{\beta}_k = -ig_1\Theta(-k)e^{i(\omega_k - \omega_e)t}\alpha_1 - ig_2 e^{i(\omega_k - \omega)t}e^{-ikr}\alpha_2. \tag{A9}$$

As expected, nothing happens with the $|\downarrow\rangle|\downarrow\rangle|0\rangle$ amplitude:

$$\zeta(t) \equiv \frac{1}{\sqrt{2}}. \tag{A10}$$

The electric field's amplitudes can be found as follows:

$$\beta_k(t) = \int_0^t d\tau[-ig_1\Theta(-k)e^{i(\omega_k - \omega_e)\tau}\alpha_1(\tau)$$
$$- ig_2 e^{i(\omega_k - \omega)\tau}e^{-ikr}\alpha_2(\tau)]. \tag{A11}$$

We can now substitute this expression to Eq. (A8) to get coupled integro-differential equations for 2LS amplitudes:

$$\dot{\alpha}_1 = -\int_{k<0} (dk)e^{-i(\omega_k - \omega_e)t} \int_0^t d\tau\big[g_1^2\Theta(-k)$$
$$\times e^{i(\omega_k - \omega_e)\tau}\alpha_1(\tau) + g_1 g_2 e^{i(\omega_k - \omega)\tau}e^{-ikr}\alpha_2(\tau)\big] \tag{A12}$$

and

$$\dot{\alpha}_2 = -\int (dk)e^{-i(\omega_k - \omega)t}e^{ikr} \int_0^t d\tau\big[g_1 g_2 \Theta(-k)$$
$$\times e^{i(\omega_k - \omega_e)\tau}\alpha_1(\tau) + g_2^2 e^{i(\omega_k - \omega)\tau}e^{-ikr}\alpha_2(\tau)\big]. \tag{A13}$$

Equations (A12) and (A13) can be further simplified by changing the integration variable over each chiral branch:

$$\int_{k>0} (dk) \to \int_0^\infty \frac{d\omega}{2\pi} \frac{1}{|d\omega/dk|}. \tag{A14}$$

Next, we neglect momentum dependence of the group velocity, $d\omega/dk \to c$, and extend frequency integrations to infinity. This allows one to derive the following equations, which are local in time (using Weisskopf approximation of the integral over frequency) (with $\frac{\gamma}{2} = \frac{g_1^2}{c}$ and $\frac{\Gamma}{2} = \frac{2g_2^2}{c}$; we also neglect the time delay, $r/c \to 0$):

$$\dot{\alpha}_1(t) = -\frac{\gamma}{2}\alpha_1(t),$$

$$\dot{\alpha}_2(t) = -\frac{\Gamma}{2}\alpha_2(t) - \frac{1}{2}\sqrt{\frac{\Gamma\gamma}{2}}e^{-i(\omega_e - \omega)t}\alpha_1(t). \tag{A15}$$

The electric field can be found as follows:

$$V(x,t) \propto i \int (dk) e^{ikx - i\omega_k t} \beta_k(t), \qquad (A16)$$

which gives for the wave propagating to the left (we also put $r \to 0$)

$$V(x, \tau = t - |x|/c) \propto e^{i\phi} [e^{-i\omega_e \tau} \alpha_1(\tau) + e^{-i\omega \tau} \alpha_2(\tau)]. \qquad (A17)$$

From there the scattered part of the field in the quantum case is given by

$$V_q(t) = a\, e^{i\phi} \sqrt{\frac{\Gamma}{2}} \frac{\sqrt{\gamma\Gamma} \left(e^{-\frac{\gamma t}{2}} - e^{-\frac{\Gamma t}{2} + i\Delta t} \right)}{\gamma - \Gamma + 2i\Delta}, \qquad (A18)$$

where $\Delta = \omega_e - \omega$ is detuning between qubits, γ is the radiative relaxation rate of SPS, and Γ is the rate for the probe qubit. ϕ denotes delay of the wave package due to the finite optical length, which can be experimentally fully removed. All signals have their own affine transformation, which mixes field quadratures, $a\, e^{i\phi}$ altering the detected signal due to the presence of the experimental environment. Therefore, solutions on the quadratures of field should be odd and even with respect to detuning between qubits; calibration of the delay could be provided assuming the resonance condition—one of the scattered field quadratures should be equal to zero. Therefore, we have only one free parameter for the subsequent analysis, namely, scaling factor, which accounts for overall attenuation and amplification in the experimental tract.

Assuming a closed bath-TLS system allows one to obtain the solution in a much more simple way using only vectors of state, which is not the case when modes of field are factorized inevitably leading to the density-matrix approach.

However, an analytical solution could be determined using an equivalent master equation [26]. Using the input-output relation for the cascaded system and assuming Markovian approximation one is able to determine density-matrix dynamics:

$$\begin{aligned}
\partial_t \rho = &-i\left[\rho, \frac{\omega}{2}\sigma_z + \frac{\omega^e}{2}\sigma_z^e + \frac{i\sqrt{\gamma\Gamma}}{2}(\sigma_+^e \sigma_- - \sigma_+ \sigma_-^e) \right] \\
&+ (\sqrt{\gamma}\sigma_+^e + \sqrt{\Gamma}\sigma_+)\rho(\sqrt{\gamma}\sigma_-^e + \sqrt{\Gamma}\sigma_+) \\
&- \frac{1}{2}(\sqrt{\gamma}\sigma_+^e + \sqrt{\Gamma}\sigma_+)(\sqrt{\gamma}\sigma_-^e + \sqrt{\Gamma}\sigma_+)\rho \\
&- \frac{1}{2}\rho(\sqrt{\gamma}\sigma_+^e + \sqrt{\Gamma}\sigma_+)(\sqrt{\gamma}\sigma_-^e + \sqrt{\Gamma}\sigma_+), \quad (A19)
\end{aligned}$$

with $\rho(0) = (\frac{|0\rangle + |1\rangle}{\sqrt{2}})(\frac{\langle 0| + \langle 1|}{\sqrt{2}}) \otimes (|0\rangle\langle 0|)$. In the Heisenberg representation such a system gives the closed system of ODEs where cross correlations between two Hilbert spaces could not be simply reduced like in effective mean field theories [30] or similar Langevin equation systems [8]. Nevertheless it is possible to find a full analytical solution for the field in the resonance case.

APPENDIX B: DERIVATION OF CLASSICAL CASE FORMULAS

The very natural approach to compare results obtained after quantum scattering is to scatter the classical field with the same waveform in time domain. One has to exponentially modulate the classical pulse by means of an arbitrary waveform generator. Due to the difference in photon statistics it is proposed that the scattered field can possess different features. But, in the limit of infinitely small drive amplitude it is expected to obtain similar behavior, since α in the coherent state would be excessively small.

We will discuss a solution of the closed system of equations of motion originating from the master equation in Linblad form. In terms of detuning Δ between the classical signal and the probe's qubit frequency and driving field force Ω one is able to formulate the task in the rotating wave approximation:

$$H = \frac{\Delta}{2}\sigma_z + \frac{\Omega}{2}e^{-\frac{\gamma t}{2}}\sigma_x. \qquad (B1)$$

With radiative relaxation rate Γ of the probe (pure Γ_1^r) one is able to write the following equations of motion using the Heisenberg picture in resonance case:

$$\begin{aligned}
\partial_t \langle \sigma_x \rangle &= -\frac{\Gamma}{2}\langle \sigma_x \rangle, \\
\partial_t \langle \sigma_y \rangle &= -\Omega \langle \sigma_z \rangle e^{-\frac{\gamma t}{2}} - \frac{\Gamma}{2}\langle \sigma_y \rangle, \qquad (B2) \\
\partial_t \langle \sigma_z \rangle &= -\Gamma(1 + \langle \sigma_z \rangle) + \Omega\, e^{-\frac{\gamma t}{2}} \langle \sigma_y \rangle.
\end{aligned}$$

The answer for $\langle \sigma_- \rangle$ contains only $\langle \sigma_y \rangle$ terms, which are nothing, but the solution of the second-order differential equation with exponential terms,

$$\begin{aligned}
4\Gamma\Omega &+ e^{\frac{\gamma t}{2}}[4y''(t) + 2(\gamma + 3\Gamma)y'(t) + \Gamma(\gamma + 2\Gamma)y(t)] \\
&+ 4\Omega^2 e^{-\frac{\gamma t}{2}} y(t) = 0, \qquad (B3)
\end{aligned}$$

where $\langle \sigma_y \rangle(t) \equiv y(t)$, $y(0) = 0$, and $y'(0) = -\Omega$. The closed system of the first-order differential equations contains time-dependent terms; however, a full analytical solution exists and fully matches numerical simulations given in the main text. We are interested in solutions depending only on Ω, where

$$\Omega \sim \gamma \sim \Gamma,$$

and we can try to provide perturbative analysis for $\langle \sigma_- \rangle$ dynamics in the time domain. Solutions for $\Omega = 0$ are pure exponents. Taking into account initial conditions one could write simple perturbation theory in order to find an asymptotic solution in terms of the functional series [higher-order terms for each order of partial sums should be $O(\Omega^{n+1})$]:

$$\begin{aligned}
\langle \sigma_y \rangle &= \sigma_y^{(0)} + e^{-\frac{\Gamma t}{2}} \sum_{n=1}^{+\infty} \Omega^n \sigma_y^{(n)}, \\
&\qquad\qquad\qquad\qquad\qquad\qquad (B4) \\
\langle \sigma_z \rangle &= \sigma_z^{(0)} + \sum_{n=1}^{+\infty} \Omega^n \sigma_z^{(n)},
\end{aligned}$$

where $\langle \sigma_y \rangle(0) = 0$ and $\langle \sigma_z \rangle(0) = -1$, which leads to $\langle \sigma_y^{(n)} \rangle(0) = 0$ and $\langle \sigma_z^{(n)} \rangle(0) = -1$ for each order of n, where
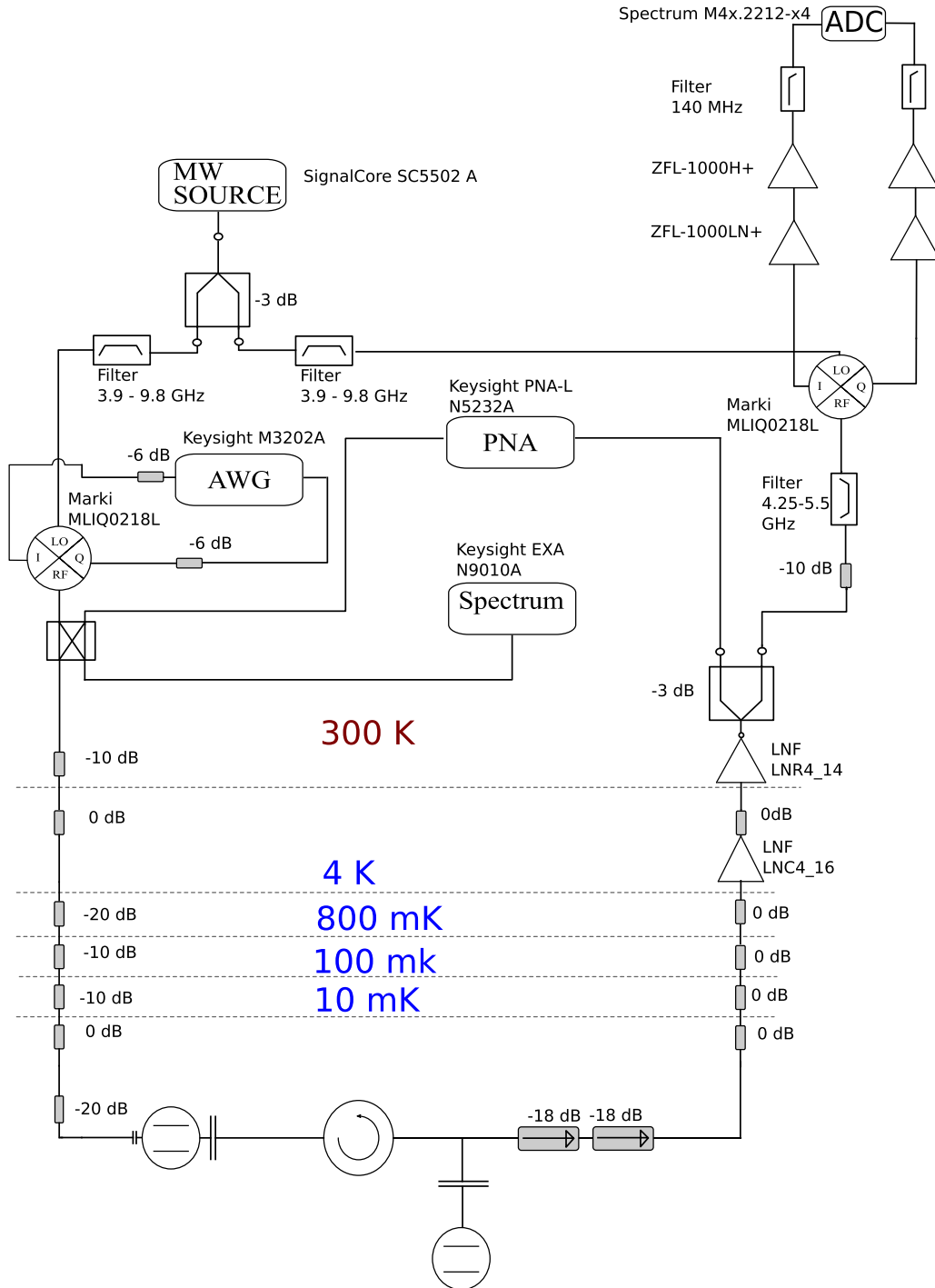
FIG. 9. Experimental setup used for time domain and frequency domain measurements. Both parts are presented: room temperature and cryogenic. Commercially available microwave devices are denoted.

$n = 0$ denotes the unperturbed solution ($\Omega = 0$). For $n = 0$ chains start from $\langle\sigma_z^{(0)}\rangle = -1$ and $\langle\sigma_y^{(0)}\rangle = 0$. Recurrence relations for the given set of series are, provided the condition of $n > 0$,

$$\partial_t\langle\sigma_y^{(n)}\rangle\Omega^n = -\Omega\, e^{-\frac{\Gamma t}{2} - \frac{\gamma t}{2}}\left(\Omega^{n-1}\langle\sigma_z^{(n-1)}\rangle\right),$$

$$\partial_t\langle\sigma_z^{(n)}\rangle\Omega^n = -\Omega^n\Gamma\langle\sigma_z^{(n)}\rangle + \Omega\, e^{\frac{\Gamma t}{2} - \frac{\gamma t}{2}}\left(\Omega^{n-1}\langle\sigma_y^{(n-1)}\rangle\right). \quad \text{(B5)}$$

Any possible correction could be determined. The first leading correction to the answer linear in Ω is

$$V_{cl}^{(1)}(t) = \sqrt{\frac{\Gamma}{2}}\frac{\langle\sigma_y\rangle}{2} = \sqrt{\frac{\Gamma}{2}}\frac{\Omega\left(e^{-\frac{\gamma t}{2}} - e^{-\frac{\Gamma t}{2}}\right)}{\gamma - \Gamma}. \quad \text{(B6)}$$

It is worth mentioning that such a formula fully matches the answer for the leading order in Ω for the scattered field in the case of reemitting not more than one photon. It could be

easily derived utilizing Moller [29] scattering amplitudes with a non-Hermitian Hamiltonian.

The second-order correction in Ω is

$$V_{cl}^{(2)}(t) = \sqrt{\frac{\Gamma}{2}} \frac{2\Omega^3 e^{-t\left(\frac{3\gamma}{2}+\Gamma\right)}\left((\gamma-\Gamma)^2 e^{\frac{1}{2}t(3\gamma+\Gamma)} + (-3\gamma^2 - 2\gamma\Gamma + \Gamma^2)e^{\frac{1}{2}t(\gamma+\Gamma)} + \gamma(3\gamma-\Gamma)e^{\gamma t} + \gamma(\gamma+\Gamma)e^{\Gamma t}\right)}{\gamma(\gamma-\Gamma)^2(3\gamma-\Gamma)(\gamma+\Gamma)}. \quad \text{(B7)}$$

Other corrections are too complex to reflect them explicitly, but nonzero and polynomially decreasing.

APPENDIX C: DETAILS OF THE EXPERIMENTAL SETUP

In our work, we utilize both the frequency domain and time domain measurements. Time domain measurements are performed by means of a heterodyne-type detection scheme with fast DACs (1 GSa/s sampling) and ADCs (1.25 GSa/s) with the typical number of experimental traces average of 2^{24} (approximately 10^7). Preliminary measurements include double callibration of the phases and amplitudes of input signals using a spectrum analyzer and double-balanced four ports mixers in the single-sideband modulation regime [27]. After the calibration of the up-converted signal to the GHz-range frequency, we proceed with the down-conversion calibration in order to avoid parasitic harmonics and phase accumulation. The typical IF frequency is 100 MHz. Our experimental setup consists of two main parts: The room part and cryogenic. Since the signal path includes both stages, it is properly attenuated and filtered; see Fig. 9. Amplification also has two stages: Cryogenic HEMT amplifier and room-part amplifiers for both quadratures. Qubits are located on two separate silicon chips and placed into two separate sample holders connected via cryogenic circulator. The output line of the probe qubit is followed by two cryogenic isolators. Frequency domain measurements (all spectroscopic measurements) are provided via network analyzer. Devices used have a common 10 MHz reference signal.

[1] A. Wallraff, D. I. Schuster, A. Blais, L. Frunzio, R.-S. Huang, J. Majer, S. Kumar, S. M. Girvin, and R. J. Schoelkopf, Nature (London) **431**, 162 (2004).

[2] A. Fedorov, A. K. Feofanov, P. Macha, P. Forn-Díaz, C. J. P. M. Harmans, and J. E. Mooij, Phys. Rev. Lett. **105**, 060503 (2010).

[3] O. Astafiev, A. M. Zagoskin, A. A. Abdumalikov, JR., Y. A. Pashkin, T. Yamamoto, K. Inomata, Y. Nakamura, and J. S. Tsai, Science **327**, 840 (2010).

[4] A. Y. Dmitriev, R. Shaikhaidarov, V. N. Antonov, T. Hönigl-Decrinis, and O. V. Astafiev, Nat. Commun. **8**, 1352 (2017).

[5] I.-C. Hoi, C. M. Wilson, G. Johansson, T. Palomaki, B. Peropadre, and P. Delsing, Phys. Rev. Lett. **107**, 073601 (2011).

[6] Z. H. Peng, S. E. De Graaf, J. S. Tsai, and O. V. Astafiev, Nat. Commun. **7**, 12588 (2016).

[7] C. W. Gardiner and A. S. Parkins, Phys. Rev. A **50**, 1792 (1994).

[8] W. V. Pogosov, A. Y. Dmitriev, and O. V. Astafiev, Phys. Rev. A **104**, 023703 (2021).

[9] B. Fan, G. Johansson, J. Combes, G. J. Milburn, and T. M. Stace, Phys. Rev. B **90**, 035132 (2014).

[10] D. Roy, C. M. Wilson, and O. Firstenberg, Rev. Mod. Phys. **89**, 021001 (2017).

[11] J.-T. Shen and S. Fan, Phys. Rev. Lett. **95**, 213001 (2005).

[12] H. Zheng, D. J. Gauthier, and H. U. Baranger, Phys. Rev. A **82**, 063816 (2010).

[13] J.-T. Shen and S. Fan, Phys. Rev. Lett. **98**, 153003 (2007).

[14] J.-T. Shen and S. Fan, Phys. Rev. A **79**, 023837 (2009).

[15] Z. Liao, X. Zeng, H. Nha, and M. S. Zubairy, Phys. Scr. **91**, 063004 (2016).

[16] D. Roy, Phys. Rev. B **81**, 155117 (2010).

[17] Y. Wang, J. Minář, L. Sheridan, and V. Scarani, Phys. Rev. A **83**, 063842 (2011).

[18] P. Domokos, P. Horak, and H. Ritsch, Phys. Rev. A **65**, 033832 (2002).

[19] B. Q. Baragiola, arXiv:1408.4447 (2014).

[20] R. J. Glauber, Phys. Rev. **130**, 2529 (1963).

[21] R. J. Glauber, Phys. Rev. **131**, 2766 (1963).

[22] K. Inomata, Z. Lin, K. Koshino, W. D. Oliver, J.-S. Tsai, T. Yamamoto, and Y. Nakamura, Nat. Commun. **7**, 12303 (2016).

[23] N. Roch, M. E. Schwartz, F. Motzoi, C. Macklin, R. Vijay, A. W. Eddins, A. N. Korotkov, K. B. Whaley, M. Sarovar, and I. Siddiqi, Phys. Rev. Lett. **112**, 170501 (2014).

[24] J. Koch, T. M. Yu, J. Gambetta, A. A. Houck, D. I. Schuster, J. Majer, A. Blais, M. H. Devoret, S. M. Girvin, and R. J. Schoelkopf, Phys. Rev. A **76**, 042319 (2007).

[25] M. Pechal, J.-C. Besse, M. Mondal, M. Oppliger, S. Gasparinetti, and A. Wallraff, Phys. Rev. Appl. **6**, 024009 (2016).

[26] C. W. Gardiner and M. J. Collett, Phys. Rev. A **31**, 3761 (1985).

[27] E. Rubiola, arXiv:physics/0608211 [physics.ins-det] (2006).

[28] M. O. Scully and M. S. Zubairy, *Quantum Optics* (Cambridge University Press, Cambridge, 1999).

[29] K. A. Fischer, R. Trivedi, V. Ramasesh, I. Siddiqi, and J. Vučković, Quantum **2**, 69 (2018).

[30] M. A. Armen and H. Mabuchi, Phys. Rev. A **73**, 063801 (2006).